ACCEPTED ARTICLE PREVIEW

Accepted Article Preview: Published ahead of advance online publication

Gate-tunable Fresnel zone plate based on single-walled carbon nanotubes for terahertz applications

Arina V. Radivon, Nikita I. Raginov, Elizaveta G. Tsiplakova, Aram A. Mkrtchyan, Gleb M. Katyba, Aleksey V. Chernykh, Ignat I. Rakov, Maksim I. Paukov, Mikhail S. Mironov, Mikhail V. Shashkov, Andrey A. Vyshnevyy, Demyan D. Rybnikov Darya R. Ilyenkova, Gennadiy A. Komandin, Kirill I. Zaytsev, Yuriy G. Gladush, Nikolay V. Petrov, Albert G. Nasibulin, Aleksey V. Arsenin, Valentyn Volkov, Dmitry V. Krasnikov, Maria G. Burdanova

Cite this article as: Arina V. Radivon, Nikita I. Raginov, Elizaveta G. Tsiplakova, Aram A. Mkrtchyan, Gleb M. Katyba, Aleksey V. Chernykh, Ignat I. Rakov, Maksim I. Paukov, Mikhail S. Mironov, Mikhail V. Shashkov, Andrey A. Vyshnevyy, Demyan D. Rybnikov Darya R. Ilyenkova, Gennadiy A. Komandin, Kirill I. Zaytsev, Yuriy G. Gladush, Nikolay V. Petrov, Albert G. Nasibulin, Aleksey V. Arsenin, Valentyn Volkov, Dmitry V. Krasnikov, Maria G. Burdanova. Gate-tunable Fresnel zone plate based on single-walled carbon nanotubes for terahertz applications. *Light: Advanced Manufacturing* accepted article preview 29 November, 2025; doi: 10.37188/lam.2026.004

This is a PDF file of an unedited peer-reviewed manuscript that has been accepted for publication. LAM are providing this early version of the manuscript as a service to our customers. The manuscript will undergo copyediting, typesetting and a proof review before it is published in its final form. Please note that during the production process errors may be discovered which could affect the content, and all legal disclaimers apply.

Received 25 August 2025; revised 14 November 2025; accepted 28 November 2025;
Accepted article preview online 29 November 2025

Accepted Manuscript

ACCEPTED ARTICLE PREVIEW

Gate-tunable Fresnel zone plate based on single-walled carbon nanotubes for terahertz applications

Arina V. Radivon Nikita I. Raginov Elizaveta G. Tsiplakova Aram A. Mkrtchyan Gleb M. Katyba Aleksey V. Chernykh Ignat I. Rakov Maksim I. Paukov Mikhail S. Mironov Mikhail V. Shashkov Andrey A. Vyshnevyy Demyan D. Rybnikov Darya R. Ilyenkova Gennadiy A. Komandin Kirill I. Zaytsev Yuriy G. Gladush Nikolay V. Petrov Albert G. Nasibulin Aleksey V. Arsenin Valentyn Volkov Dmitry V. Krasnikov Maria G. Burdanova*

Arina V. Radivon, Maksim I. Paukov, Mikhail S. Mironov, Aleksey V. Arsenin, Maria G. Burdanova
Moscow Center for Advanced Studies, Kulakova str. 20, Moscow, 123592, Russia
Demyan D. Rybnikov, Darya R. Ilyenkova, Gennadiy A. Komandin, Kirill I. Zaytsev, Maria G. Burdanova
Prokhorov General Physics Institute of the Russian Academy of Sciences, Moscow, 119991, Russia
Gleb M. Katyba, Maria G. Burdanova
Institute of Solid State Physics of the Russian Academy of Sciences, Chernogolovka, 142432, Russia
Nikita I. Raginov, Ignat I. Rakov, Dmitry V. Krasnikov, Albert G. Nasibulin, Aram A. Mkrtchyan, Yuriy Gladush
Skolkovo Institute of Science and Technology, Moscow, 121205, Russia
Elizaveta G. Tsiplakova, Aleksey V. Chernykh, Nikolay V. Petrov
ITMO University, St. Petersburg, 191002, Russia
Nikolay V. Petrov
Qingdao Innovation and Development Center Harbin Engineering University, Qingdao, 266000, China
Mikhail V. Shashkov
Boreskov Institute of Catalysis SB RAS, Novosibirsk 630090, Russia
Andrey A. Vyshnevyy, Aleksey V. Arsenin, Valentyn Volkov
Emerging Technologies Research Center, XPANCEO, Dubai Investment Park First, Dubai, United Arab Emirates
Email Address: burdanova.mg@gmail.com

Keywords: *Single-walled carbon nanotubes, terahertz lens, tunable optics, focus intensity modulation, ionic-liquid gating, electrical modulation*

The active manipulation of electromagnetic waves through electrical tuning of nanomaterials is a key advantage for modern technology. We employed the tunable optical response of ionic-liquid-gated single-walled carbon nanotube (SWCNT) films to address a major challenge in terahertz (THz) optics – the limited range of materials with suitable optical properties. In this study, we demonstrated a high-performance THz intensity modulator combined with a focusing Fresnel zone plate (FZP) integrated in electro-chemical cell. We introduce a new approach for designing and fabricating the FZP, based on pre-measured dielectric properties of SWCNT films under applied voltage. The superior shielding effectiveness (up to 8×10^8 dB cm^2 g^{-1}) of SWCNT films enables the creation of an ultrathin terahertz lens. Electrical gating doubled the minimum refractive index, enhancing lens performance. This also enabled *in situ* tunability of the intensity modulation depth, from +15 to –20 %, with an applied voltage of +2 to –2 V. Although the current switching time is 3.6 seconds, our work presents the first demonstration of an electrochemically gated SWCNT FZP, offering distinct advantages in tunability and thin-film design. Operating at 327 GHz, this FZP is a promising solution for novel adaptive THz communication devices.

Accepted Manuscript

1 Introduction

The remarkable properties of THz waves have inspired the development of numerous emerging applications. High frequencies present the potential for enhanced channel capacities in 6G and beyond wireless communications. The long-wavelength electric dipole vibrations of many molecules and crystals are in the THz range, making a wide range of applications possible in chemical identification, material characterisation, atmospheric/astrophysics studies, and gas sensing [1, 2, 3, 4, 5]. Owing to its non-ionising

ACCEPTED ARTICLE PREVIEW

nature, THz radiation is a powerful tool for non-destructive control [6], security screening [7], weapon detection [8], biomedical imaging [9], and delicate investigation of cultural heritage artifacts [10].

Due to the broad applicability of THz radiation, efforts have been made to improve the performance of optical elements to meet the demands of THz applications. The most common lens- or mirror-based THz focusing systems have limited focal spot quality and energy efficiency or provide a trade-off between these two important parameters [11]. One of the current trends in optical element design is the reduction in thickness [11]. Historically, aberrations have been corrected with aspheric shapes or multilens designs, leading to heavy and complex systems [12, 13, 14]. Consequently, the development of ultra-thin lenses is crucial, and Fresnel zone plates (FZPs) are a viable solution. Despite advances in diffraction optics, most FZPs remain non-switchable. However, for emerging applications, such as computational THz imaging and sensing [15], light detection and ranging [16], and dynamic holography, it would be desirable to control the optical elements.

From this point of view, significant improvement of the THz optics performance has been achieved by the electrical tunability of nanomaterial properties. Among the various techniques, electrochemical gating paves the way for the gating of porous bulk nanomaterials. For example, ionic-liquid gating on a graphene modulator has shown an improved amplitude modulation depth of up to 99 % in the transmission mode under an applied voltage as small as +3 V [17]. By controlling the electrolyte–graphene interface gap in the quarter-wavelength cavity structure and utilising the resonance effect, a 40 % modulation depth was reached in the reflection mode in the [−0.5, +0.5] V range [18]. In these studies, the ionic liquids created an electrical double layer at the graphene interface, which could adjust the intraband transition of carriers, even under a small applied bias. Similarly, carbon nanotubes, graphene counterparts, show a Fermi level shift of over 1.2 eV, even at low biases ($\sim$ 3 V) [19]. The combination of strong electrostatic doping of single-walled carbon nanotubes (SWCNTs) with their intrinsically high conductivity [20] opens a new direction for device improvement. However, to the best of our knowledge, the potential of SWCNT films as electrochemically tuned THz optoelectronic devices has not been discussed or considered in previous studies.

In this study, we manipulated the intensity of the beam that passes through a transmission type THz SWCNT-based FZP with active ionic-liquid gating. This is possible owing to advanced technologies. for nanotube production and patterning combined with ionic-liquid gating. To predict the FZP performance, we first performed spectroscopy of the separate conventional ionic-liquid gating cell. The gating of SWCNT films led to a two-fold increase in their refractive index upon change of the bias voltage from –2 to +2 V. Next, we employed a new and robust chemical-free method for the deposition of patterned carbon nanotube films for dry transfer onto a z-cut quartz substrate. Our FZP with nanometer thickness showed intense focusing efficiency with a diffraction-limited lateral size of 1.14λ. The encapsulation of FZP in an electrochemical cell enabled the tuning of the FZP focal spot intensity from −20 to +15 %. This approach suggests a new direction for the design of SWCNT-based THz optics.

2 Concept

Figure 1 shows a schematic design of the proposed tunable lens. The lens comprised a thin SWCNT film, FZP, with an ionic liquid sandwiched between two z-cut quartz substrates. The expression for the zone is as follows: $r_n^2 + f^2 = \left(f + n\frac{\lambda}{2}\right)^2$, where n is the zone number, r_n is the outer radius of the n-th zone, f is the focal distance, and λ is the working wavelength. For a practical implementation, we engineered an FZP with a focal length of 2 cm and $N = 10$ at $\lambda = 917$ μm ($\nu = 327$ GHz). The lens is 28.6 mm in diameter and consists of five concentric rings. The lens size was chosen to cover the full width of the beam and avoid fabrication limitations (see SI S4 for details). The same lens could be used at both higher and lower frequencies. At higher frequencies, the focus point was extended. For 300 μm (1 THz) the focus will be at 6.2 cm, for 150 μm (2 THz) at 13 cm and for 100 μm (3 THz) at 19.5 cm. Interconnections through small stripes ensured a uniform doping distribution. To enable dynamic electrical control of the lens properties, four arc-shaped contacts were deposited using thermal evaporation, consisting of a 5 nm layer of titanium and a 50 nm layer of gold. Two of these electrodes were connected to the SWCNT FZP,

Accepted Manuscript

ACCEPTED ARTICLE PREVIEW

whereas the remaining two served as counter electrodes for gating. The ionic liquid utilised was 1–Butyl–3–methylimidazolium bis(trifluoromethylsulfonyl)imide (BMIM NTf2), which was chosen for its large electrochemical window of stability and tolerance to the ambient atmosphere. Patterned films for the FZP were fabricated via aerosol chemical vapour deposition[21]. SWCNTs serve as opaque regions in the FZP design[22, 23]. The fabrication process involves laser-etching a stainless-steel plate to create a 150-200 μm stencil, which is then pressed onto a nitrocellulose filter using rollers to selectively compress the areas. The SWCNT aerosol was then deposited onto uncompressed filter areas, creating a nanotube film that matched the stencil geometry, followed by a dry transfer [24] onto a quartz substrate.

Figure 1a (right-hand side) illustrates the basic concept of the proposed flat FZP, in which the applied voltage tunes the intensity of the focal spot intensity. When a uniform plane wave radiated through the FZP, part of the incident radiation was partially blocked (absorbed and reflected) by the SWCNT zones, experiencing both amplitude and phase modulation. Figure S9 shows that the phase modulation under ionic gating is negligible ($<5°$), whereas the amplitude changes dominate. Focusing is the result of the constructive interference (in the focal plane) originating from different Fresnel zones. Under these conditions, amplitude modulation makes a substantial contribution to the focusing performance, making the amplitude FZP rather than the phase. In our case, the focal spot intensity at the shadow side of the lens was reached owing to the alteration of the effective SWCNT refractive index, whereas the refractive index of the ionic liquid remained unchanged (Figure S1). This modification is possible because of the adjusted intraband transition appearing under small applied biases when a large double layer is formed at the interface of the ionic liquid and SWCNT rings. The difference in the complex refractive indices between the transparent regions and those filled with SWCNT is substantial, resulting in a minimum phase change, which is necessary for constructive interference (regions I and IV in Figure 1e) and region IV in Figure S8 [25].

In our study, we utilised Raman microscopy (Setup details present in the Experimental section) to explore the gate-tunable response of SWCNT films. The spectral profile and frequency of the Raman-active G band are known to be sensitive to variations in the Fermi energy [26]. By recording the G-mode intensity (at the G-mode frequency corresponding to each voltage) across the entire active region of the device, both with and without applied voltage, we gained insight into the doping-level distribution. Figure 1b (top right corner) presents an optical image of the fabricated FZP alongside the Raman maps at applied voltages of +2, 0, and −2 V (top left, bottom left, and bottom right corners, respectively). The application of voltage led to a notable suppression of the intensity compared with 0–V, with a nearly uniform distribution across the FZP area. The observed differences in the Raman map intensities from +2 to −2 V are attributed to the intrinsic downshift of the Fermi level, likely owing to the oxygen-induced p-doping that naturally occurs under ambient conditions [27]. Further changes in voltage led to the displacement of the Fermi level downward or upward in metallic and semiconducting SWCNTs, depending on the sign of the voltage (Figure 1d. Literature indicates that for the classical rectangular scheme used in our measurements, each 1 V shift alters the Fermi level by 0.45 eV[19]. In our case, the samples are already p-doped due to the oxidation that naturally occurs in air, which shifts the Fermi level by 0.1 eV towards the valence band. Therefore, we expect that for the voltage range of [-2; +2] V, there will be a variation of the Fermi level from -1.2 to 0.8 eV (red lines in Figure 1d).

The experimental verification of the produced THz FZP lens functionality was performed using the custom-made THz continuous-wave imaging setup. As the THz source, we employed a backward wave oscillator (BWO) operating at a frequency of 327 GHz (Figure 1c) (further details of the experimental setup can be found in the Experimental section). Our specific beam waist selection represents a carefully considered compromise. A wider beam interacts more strongly with the radial gold electrodes in our device architecture, introducing unwanted effects. Conversely, positioning these electrodes at greater radial distances to accommodate a larger beam would diminish the electrochemical doping efficiency because of the increased separation between the electrodes and active regions of the FZP. We would like to highlight that two samples were studied in this work: the ionic-liquid-gated cell and the ionic-liquid-gated FZP, working as tunable lenses. The ionic-liquid-gated FZP geometry is more complex. However, they retain the performance of conventional electrochemical cells. For simplicity, we refer to it as the "ionic-

Accepted Manuscript

ACCEPTED ARTICLE PREVIEW

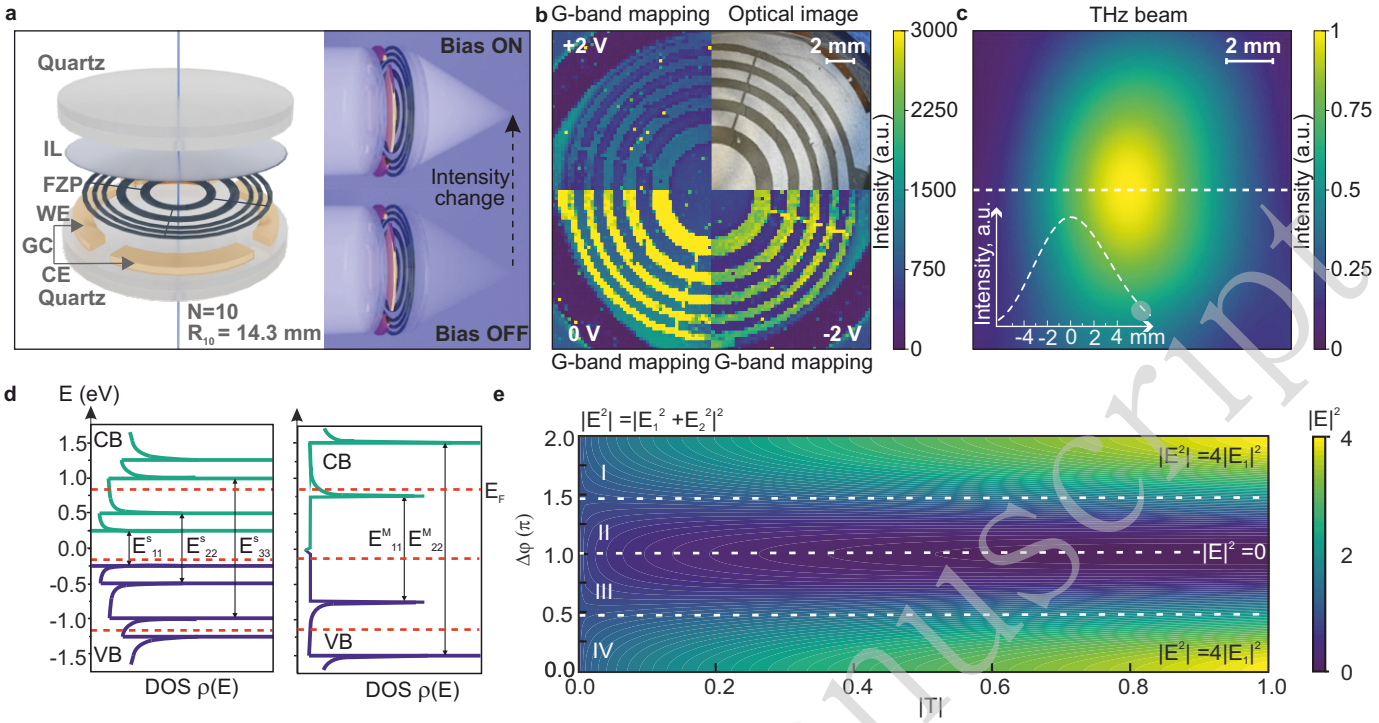

Figure 1: a) Concept of the device structure. A thin ionic liquid layer coats a thin Fresnel zone plate based on SWCNT encapsulated between two z-cut quartz substrates and connects to the FZP with two gold contacts (GC). The working and counter electrodes are denoted as WE and CE, respectively. The FZP consists of 10 zones, with an external radius of 14.3 mm. Gate-induced change of the dielectric properties of the carbon nanotube film results in the change of the radiation intensity in the FZP focus. b) The photo of the fabricated SWCNT FZP (upper right corner) alongside Raman intensity maps at applied voltages of +2, 0, and −2 V (at the G-mode frequency corresponding to each voltage). The opaque zones in the optical image are SWCNTs. c) The THz spot without FZP measured with a Golay cell and shown in normalised units. d) Electronic properties of semiconducting (left) and metallic (right) SWCNT, each with an approximate diameter of 2 nm. VB denotes valence band, CB represents conduction band, and DOS denotes density of states. The estimated maximum and minimum shifts of the Fermi level are highlighted with dashed red lines. e) The interference of two coherent beams calculated to understand the role of amplitude and phase modulations.

liquid gated FZP" rather than the "ionic-liquid gated FZP cell".

3 Results

3.1 Ionic-liquid gated cell spectroscopy

To underscore the significance of the changes in the SWCNT dielectric response during the operation of the flat lens based on FZP, we conducted separate spectroscopic measurements of continuous carbon nanotube films using THz Time-Domain Spectroscopy (THz-TDS). Electrochemical gating was achieved using the distinct two-electrode cell configuration shown in Figure 2. This device consists of two z-cut quartz substrates filled with an electrolyte (ionic liquid). Gold strips were employed to bias a SWCNT film electrode with a 5×10 mm^2 film electrode. Upon applying a bias voltage between the sample and counter electrode, positive and negative ions (depending on the voltage sign) from the electrolyte accumulate near the SWCNT film, forming an electric double layer.

To assess the cell performance, cyclic voltammetry tests were performed at the scan rate of 100 mV/s over the potential range from −2 to 2 V (Figure 2b,c). A constant potential was maintained for 3 min until a steady-state current was reached, and optical measurements were conducted. The dependence of the real n and imaginary k parts of the effective refractive index of SWCNT in the cell on the bias voltage is shown in Figure 2b. This voltage-induced change can be understood through three possible band alignment scenarios. In the first case, without a gate voltage, the Fermi level was slightly below the neu-

Accepted Manuscript

ACCEPTED ARTICLE PREVIEW

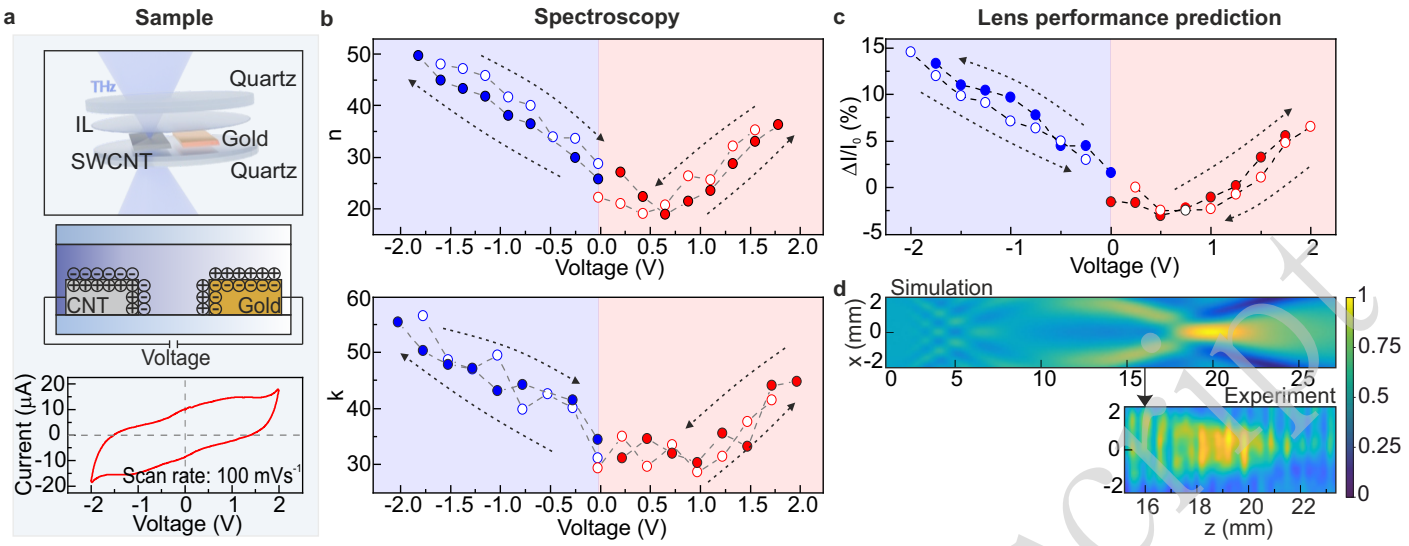

Figure 2: a) From top to bottom: schematic view of the gated SWCNT film in an electrochemical cell; scheme of the operational principle of the ionic-liquid gating inside an electrochemical cell—charged molecules screen the Coulomb potential of SWCNT film and gold pad; results of the cyclic voltammetry studies of the SWCNT films recorded at v= 100 mV/s. b) The effective refractive index change of SWCNT films over the voltage range of [−2,+2] V (same as in cyclic voltammetry). The direction of the voltage sweep is denoted by arrows. Solid circles represent the forward direction and hollow circles—backward direction. c) The modulation depth of the lens intensity, extracted from simulation, is plotted versus voltage. d) The field intensity at 327 GHz transmitted behind the designed Fresnel zone plate in the case of a simulation and experiment at 0 V.

tral point, indicating p-doping due to oxygen or water adsorption under ambient conditions. This was manifested in our experiments by the shift of the refractive index minimum towards positive values. To adjust the Fermi level to a neutral point, it is necessary to apply voltages of +0.5 to +1 V, depending on the specific position in the cyclic voltammetry. In the second scenario, the application of positive voltages effectively shifts the Fermi level toward the conduction band. In the third scenario, the application of negative voltages resulted in a shift in the opposite direction, moving the Fermi level toward the valence band. With the shift in the Fermi level from the neutrality point, the free carrier density in nanotubes increases, leading to enhanced intraband optical absorption.

The pronounced hysteresis loops observed in cyclic voltammetry are mirrored in the behaviour of the effective refractive index of SWCNT in the cell. Two local minima, approximately +0.5 and +1 V, were apparent in both the forward and backward sweeps within the positive voltage regime. This illustrates a distinct difference in the Fermi level positions when the same voltage is applied in both the forward and reverse directions. Figure 2c shows the transmitted intensity simulating the focusing performance of a hypothetical lens based on FZP, which has an effective refractive index of SWCNT in the cell extracted from spectroscopic measurements. The simulated focus position at 20 mm matched the experimental position well. Using the effective refractive indices of SWCNT in the cell over the whole voltage sweep, we calculated the relative change of the intensity as $\Delta I/I = [I(V) - I(V = 0)]/I(V = 0)$ (Figure 2). If $I(V) > I(0)$, the MD is positive, indicating an increase in intensity. If $I(V) < I(0)$, the MD is negative, indicating a consequent decrease in intensity. The intensity modulation in the focus position exhibited hysteresis behaviour, which reflected the refractive index change under the applied voltage. Overall, the modulation from approximately −5 to +15 % demonstrates the benefit of integrating ionic-liquid gating in the SWCNT FZP.

To illustrate the voltage-dependent THz optical properties, we performed THz imaging of a cloverleaf structure coated with our SWCNT films (Figure 3a). We observed a significant decrease in the transmission (CNT films on their own) as the voltage was varied toward +2 or −2 V, which manifested as a gradual suppression in the detected reflection mode intensity. The densely packed structure of the SWCNTs combined with their high refractive index allowed for a remarkable amplitude transmission of 0.7 at 0 V, even with a film thickness of 40 nm. We calculated the frequency-dependent EMI shielding ef-

Accepted Manuscript

ACCEPTED ARTICLE PREVIEW

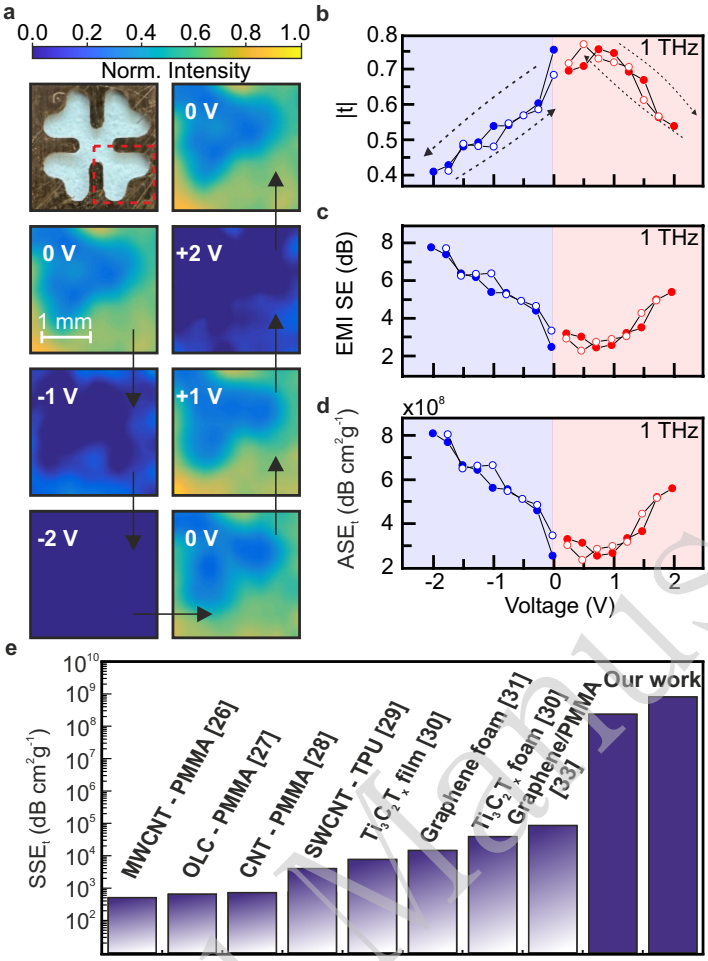

Figure 3: The optical image (in the left corner) and the THz image of the metallic cloverleaf, which is covered by a SWCNT ionic-liquid cell. The cell is comparable in size to the beam. These images were obtained under an applied voltage that varied from -2 to +2 V. The THz images collected in reflection mode correspond to the area indicated by the red square in the optical image. Importantly, the metallic area around the cloverleaf reflects the THz radiation, which is also modulated by the CNT modulator. The same scale bar is used for all images. b) The amplitude of the transmission change of SWCNT films on their own (without cloverleaf) over the voltage range of [−2,+2] V. c) and d) The corresponding electromagnetic interference shielding effectiveness (EMI SE) and absolute shielding effectiveness (ASE) calculated from (b). e) Comparison of the ASE with reported CNT, Graphene, MXenes nanocomposites taken from literature [28, 29, 30, 31, 32, 33, 34, 35]. Last two columns highlighted the results from our work for +0.5 and −2 V. MWCNT – multi-walled carbon nanotubes, OLC – onion-like carbon; PMMA – poly(methyl methacrylate), TPU – thermoplastic polyurethane.

ficiency, defined as $SE = -20log_{10}(\frac{|E_{sample}|}{|E_{reference}|})$, where $|E_{sample}|$ is the amplitude of the signal through the sample and $|E_{reference}|$ is the amplitude of the signal from the reference. As the voltage changed, we observed a two-fold reduction in transmission, leading to a four-fold increase in the effectiveness of the electromagnetic shielding, which ranged from 2 to 8 dB at 1 THz (Figure 3c). Considering the density ρ of the SWCNT films at 2.4 mg/cm^3[36] and thickness d of 40 nm, we calculated the ASE as $ASE = SE/(\rho d)$ of these aerosol-grown SWCNT films at the same frequency (Figure 3d). Notably, the ASE values for these films were significantly higher than those reported for most other nanomaterials (Figure 3e). The highest value of approximately 10^9 dB cm^2 g^{-1} is achieved at −2 V of gate voltage. This result is three orders of magnitude greater than that observed for graphene–PMMA composites owing to their high conductivity. This enhanced shielding effectiveness signifies that lightweight, low-thickness SWCNT films hold substantial promise for applications in high-performance electromagnetic shielding in the THz range.

Accepted Manuscript

ACCEPTED ARTICLE PREVIEW

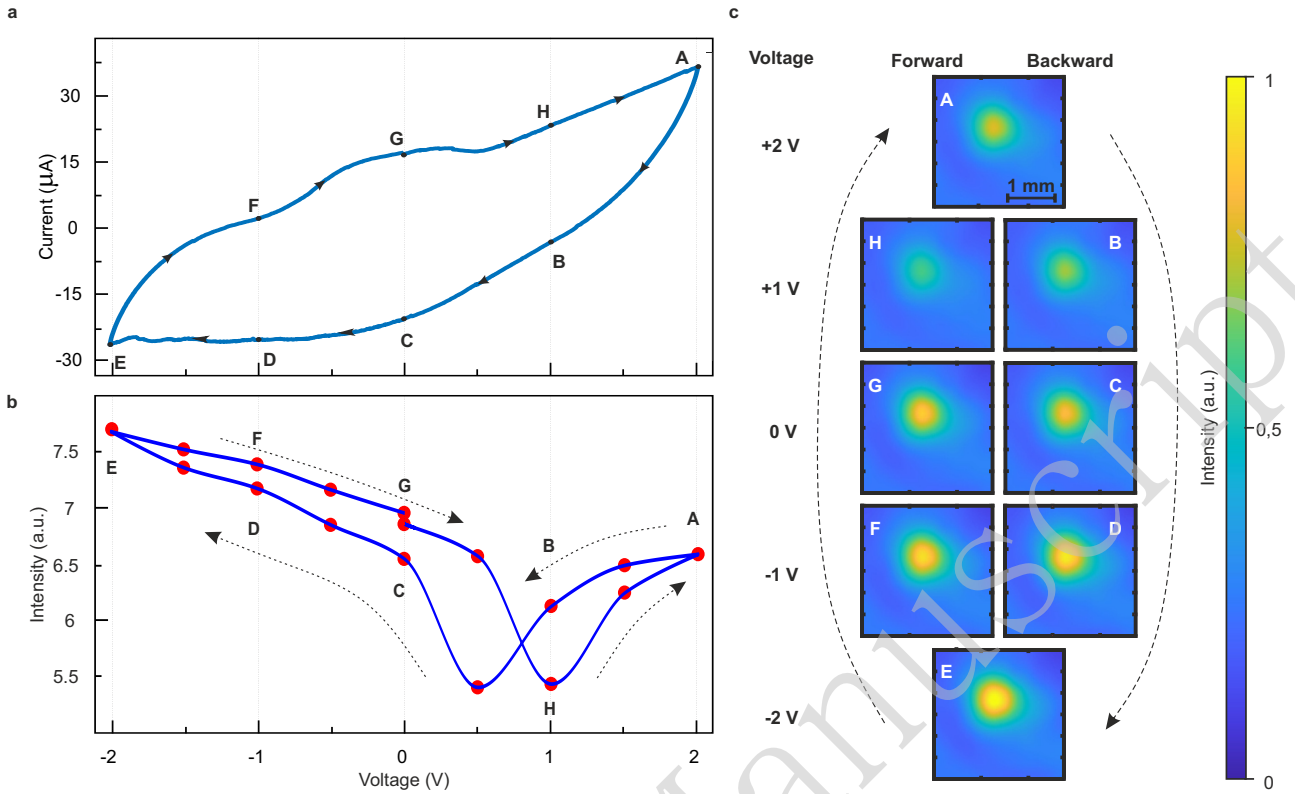

Figure 4: Focusing performance of the fabricated FZP. a) Cyclic voltammetry of the FZP. b) Change in the focal spot intensity of the lens, based on FZP (red dots) for the voltage bias in the range of −2 to 2 V with the step of 0.5 V. The solid blue line is provided for clarity. c) The intensity images at the focus position with blue and yellow representing the low and high intensity respectively. The intensity at −2 V is normalised to 1.0. The intensity takes the minimum values at +1 and the maximum at −2 V.

3.2 Ionic-liquid gated FZP performance

Encouraged by the significant tunability of the refractive index, we fabricated an SWCNT FZP using the proposed design framework. Initially, we evaluated the performance characteristics of the FZP by applying a voltage bias ranging from −2 to +2 V in a cyclic voltammetry setup (Figure 4a). We conducted experimental measurements of beam intensity at 327 GHz. The observed asymmetric intensity behaviour (Figure 4b) closely resembles the calculated response depicted in Figure 2c. No difference was observed when the voltage was applied in clockwise and counterclockwise voltage sweeps (Figure S5). This discrepancy arises from the difference in the geometry of the two-rectangle electrode cell used in the simulations and the final FZP device. Notably, the intensity decreased at voltages of +0.5 and +1 V, similar to the decrease shown in Figure 2b. The complete experimental intensity distribution across the focus spot is shown in Figure 4c. This revealed a discernible trend of gradual intensity variation. Consequently, the beam width and focal position remained constant under voltage modulation.

We demonstrated the active manipulation of the light intensity in the focus position of SWCNT FZP. Figure 5a shows the lateral intensity profiles at the four bias voltages. The slightly asymmetric shape of the cross-section may be a sign of imperfections during fabrication. Despite the intensity modulation, FWHM was found to be almost independent of the applied voltage. Meanwhile, a negative voltage tended to narrow the Rayleigh range slightly, whereas a positive voltage produced the opposite effect (Figure S3). FZP showed highly stable wavelength-scale (1.14λ) focusing resolution. A reproducible switching behaviour was observed when impulse voltages of +0.5 and +1.5 V were applied. The average response time of the device, both during the rise and fall, consistently stood at 3.6 s (Figure 5c), obtained as the lifetime of the single-exponential fit. The modulation speed, calculated as the switching frequency $MS = 1/\tau$ for our device, was 0.28 Hz. This slow response is attributed to complex ion

Accepted Manuscript

ACCEPTED ARTICLE PREVIEW

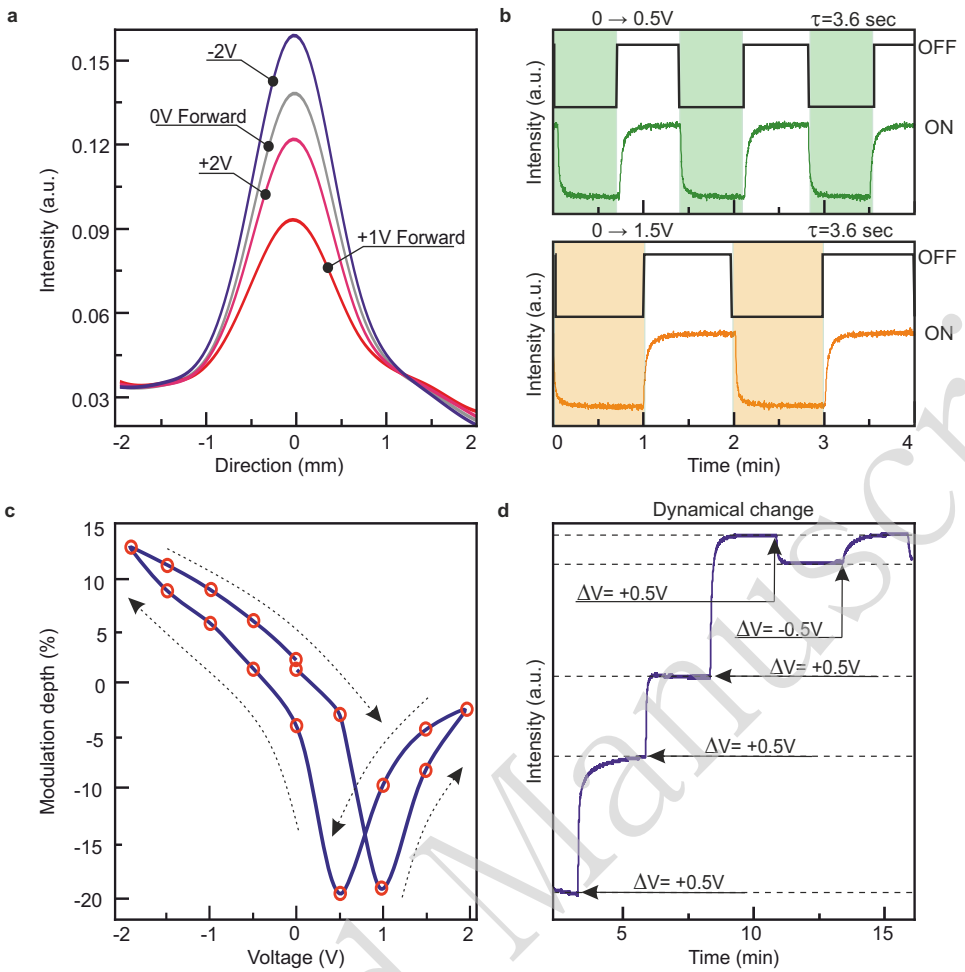

Figure 5: Gate-tunable properties of the device. a) Measured lateral intensity distributions at 0, +1, +2 and −2 V. b) Time traces of the intensity at 0 to +0.5 V and 0 to +1.5 V sweep, every 40 and 60 seconds. c) Calculated modulation depth of the FZP. d) The dynamical time traces with continuous change with 0.5 V.

transport-limited formation processes, which can be mitigated by adopting solid-state gating techniques. Moreover, a continuous random ramp-up and ramp-down of the voltage in 2.5-minute increments was conducted (Figure 5d, approximately 13 min), demonstrating its stability over prolonged voltage cycling (Figure 5d).

4 Discussion

The proposed lens concept, which utilises ionic-liquid-gated FZP based on thin SWCNT films, presents a novel and valuable solution for highly efficient and integrable adaptive THz optics. Leveraging computational control for adaptive optics can lead to real-time optimisation of lens parameters based on environmental conditions and imaging requirements. It can facilitate autonomous focus and intensity adjustments and improve performance in dynamic settings. This advancement has opened a plethora of applications, including computational imaging and sensing. The benefits that can be obtained using intensity-tunable FZPs can be enhanced by the focus-tunable approach, which was introduced in our earlier work on stretchable devices [22]. The possibility of joint control of the real and imaginary parts of the reflective refractive index of SWCNT through electrochemical gating, as revealed in this study, allows the simultaneous modulation of the amplitude and phase of the passing THz wave, opening wide possibilities for the development of dynamic spatial modulators to obtain a variety of target complex wavefronts [37]. Possible tasks include controlled focusing, aberration correction [38], pattern formation for THz single-

Accepted Manuscript

ACCEPTED ARTICLE PREVIEW

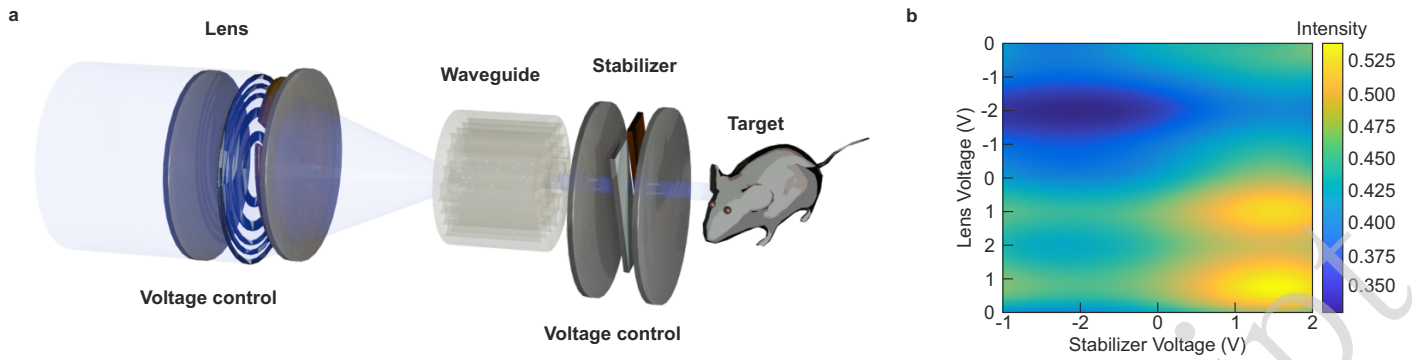

Figure 6: a) The schematic illustrates a dual-modulation architecture for precise THz radiation delivery. The system integrates two key control elements: an adjustable FZP preceding a photonic crystal waveguide, and an electrochemical cell (stabiliser) positioned after it in front of envisioned target. This sequential arrangement enables dynamic control over the beam's intensity under lens and cell voltage control through the waveguide structure, as depicted in (b).

pixels [39], and ghost imaging [40]. Thus, this study can significantly increase the adaptability of optical systems for various applications in the THz range. Furthermore, the implementation of advanced gating schemes featuring local and interleaved gating electrodes may significantly expand the range of tunable functionalities. In addition, the possibility of FZP ring adjustment holds great promise for the development of multi-focus lenses that are in high demand for super-resolution imaging.

A comparison of the present work on the dynamic control of THz waves with published studies highlights their distinctive advantages in terms of performance and practical viability. In particular, our device offers a balance between modulation depth (35%), fabrication simplicity, scalability, and additional focusing functionality. Although graphene-based modulators achieve faster switching (e.g. 0.1 ms), they require complex cleanroom-based fabrication processes[41]. In [42, 43] turn-on delays below 1 ms were reported in metamaterial-based systems, but still lacked scalability owing to the complex fabrication. In contrast, our method demonstrates enhanced large-scale fabrication potential through cost-effective processes that are suitable for industrial applications. Furthermore, compared with [44] and [18], who focused on high-resolution near-field THz imaging with a limited dynamic range, our device provides a remarkable attenuation efficiency of 8×10^8 dB cm^2 g^{-1}, enabling more robust non-destructive imaging. A promising direction for improving a single device is to increase the thickness of the CNT film. Additionally, it is possible to deposit two FZPs on separate quartz substrates facing each other in a sandwich-like structure with an ionic liquid as the separator. This structure doubled the modulation depth, similar to that of a graphene modulator[17].

Unlike conventional lithography-based metamaterials, our CNT-based approach offers significant advantages in terms of scalability and cost-effectiveness. CNT films produced using the aerosol (floating catalyst) chemical vapour deposition method potentially enable high-throughput production at substantially lower costs than traditional cleanroom fabrication processes. The inherent stretchability of our CNT films provides an additional degree of freedom for device functionality, allowing the mechanical tuning of the focus point, as demonstrated in [22]. This mechanical tunability combined with electrical modulation via ionic-liquid gating, offers a unique hybrid control mechanism that is not readily available for conventional rigid metamaterial structures. Although we achieved modulation depths comparable to other metamaterial approaches, our device architecture maintained its performance across a broader frequency range because it did not rely on resonant structures with inherently narrow-band responses.

The proposed THz system with dynamic modulation capabilities represents a significant advancement in precision imaging and biological applications. The incorporated dynamic modulators demonstrate superior resolution and an enhanced signal-to-noise ratio compared to conventional static modulation approaches, while maintaining a high temporal resolution in the dynamic operation mode[45]. These performance characteristics make the system particularly valuable for applications requiring the precise spatiotemporal control of THz radiation. Extensive experimental studies have established the profound effects of terahertz radiation on cellular processes, particularly on the regulation of genes associated with

Accepted Manuscript

ACCEPTED ARTICLE PREVIEW

stress responses, inflammation, cell cycle control, and programmed cell death and growth([46, 47]). Notably, a significant modulation was observed in the expression profiles of heat shock proteins, inflammatory cytokines, and growth factors under controlled terahertz exposure. However, achieving reproducible biological effects requires addressing several technical and methodological challenges primarily related to the precise control of exposure parameters. To overcome these limitations, we designed and implemented an advanced optical setup featuring dual electrochemical modulation elements: a gated lens positioned before the photonic crystal waveguide, and a stabiliser cell positioned after it (Figure 6a). A photonic crystal waveguide, previously optimised for targeted THz radiation delivery [48], works in concert with these elements to enable precise control over both the spatial distribution and intensity of THz radiation. By independently adjusting the voltages applied across the lens and stabiliser contacts, we achieved accurate control over the THz beam parameters (Figure 6b), enabling future systematic investigation of dose-dependent biological responses. Intensity mapping demonstrates the sophisticated interplay between two independent control parameters: the voltage applied to the adjustable lens and that applied to the stabiliser. In addition, the SWCNT-based tunable FZP demonstrated in this study holds significant promise for advanced photonic applications, particularly in self-homodyning detection and laser feedback interferometry, provided that the response time is improved[49].

5 Conclusion

In summary, we developed an intensity-tunable planar ultra-thin lens device in which the focus intensity can be electrically controlled via electrochemical gating. It was possible due to the unique optical properties of SWCNT thin films exhibiting pronounced gate-tunable intraband absorption in the THz frequency range. In particular, it was achieved due to remarkable shielding effectiveness, reaching up to 8×10^8 dB cm^2 g^{-1} at low density (2.4 mg/cm^3) and thickness (40 nm). Using this feature, we achieved a variation in the modulation depth from -20 to $+15$ %. Simultaneously, the device maintained the same focal position (Figure S7), and FWHM did not vary significantly for all the applied biases. Overall, the results demonstrate the role of electrochemical doping in the operation of thin optical elements, providing a promising area for future implementation in THz systems.

6 Materials and methods

Patterned SWCNT Thin Films:
Patterned thin films of single-walled carbon nanotubes for FZP were fabricated using the aerosol (floating catalyst) chemical vapour deposition method [21], which is based on CO decomposition through the Boudouard reaction occurring on the surface of Fe-based catalyst aerosol particles. The SEM image of the pristine SWCNT film shows the morphology of the randomly oriented SWCNTs composed of the FZP (Figure S6). The patterning procedure described here employs SWCNT films as opaque regions of the FZP, as developed elsewhere [22, 23]. Initially, a custom pattern for the FZP was etched into a stainless-steel plate using pulsed laser ablation, resulting in a rigid stencil with a height difference of 150–200 μm. Subsequently, the pattern was imprinted onto a nitrocellulose filter (HAWP, Merck Millipore, with a pore size of 0.45 μm) by passing the filter affixed to the metal stencil through rollers to compress specific pore areas, thereby reducing throughput. The areas of the stencil containing the engravings left the nitrocellulose filter unaffected. Subsequently, the SWCNT aerosol was deposited onto the uncompressed areas of a nitrocellulose filter to create a thin nanotube film that mirrored the geometry of the metal stencil. Finally, the resulting film was dry-transferred onto a quartz substrate [24]) onto a quartz substrate (Figure S4). The ionic liquid, BMIM NTf_2, was produced using a standard procedure described elsewhere[50]. Briefly, the alkylation of 1-methylimidazole by 1-bromobutane was followed by anion exchange with lithium bistriflimide in water. The choice of BMIM NTf2 as the ionic liquid is crucial for several reasons, as demonstrated in our control experiment comparing the CNT–FZP device performance with and without an ionic-liquid layer [22]. While the cell showed superior focusing performance even

Accepted Manuscript

ACCEPTED ARTICLE PREVIEW

without an ionic liquid, achieving efficient carrier density modulation under a low-voltage bias would be significantly challenging without it. The electrochemical stability window of BMIM NTf2 is particularly wide ([-2,+2]V), which is crucial for reliable operation without degradation under an applied voltage bias [51], and its stability in air is another critical practical advantage not found in many other ionic liquids [52]. BMIM NTf2's optical properties are particularly suitable for this application because of its transparency across broad THz ranges and stability under an applied voltage (Figure S1), which is essential for maintaining high transmission efficiency while enabling the desired electrochemical effects, with such transparency being rare among other ionic liquids and critical for device operation. The average response time of the device, both during rise and fall, is obtained as the characteristic time constant τ of a single-exponential fit in the form of $I = I_0 + Ae^{-t/\tau}$ where I_0 is the baseline current and A is the amplitude of the exponential component.

Spectroscopy Experimental Setup:
Raman mapping was performed using a confocal scanning Raman microscope (Horiba LabRAM HR Evolution, HORIBA Ltd., Kyoto, Japan) with a 532 nm laser wavelength (with a spectral resolution of 0.5 cm^{-1}). Measurements were carried out using linearly polarised excitation at wavelengths of 532 nm, an 1800 lines/mm diffraction grating, and $\times 10$ objective. The spot size is approximately 0.4 μm. The samples were mounted on motorised stages which allowed for a 2D x–y scan.
We employed a custom-built (GPI RAS) transmission-mode terahertz (THz) pulsed spectrometer for THz spectroscopy. This system utilises a pair of photoconductive antennas for emission and detection of THz pulses. To mitigate the effects of water vapour in the laboratory environment, the THz beam path was maintained under vacuum at approximately 10^{-3} mbar. The spectrometer operates within a spectral range of 0.05–2.5 THz and achieves a spectral resolution of up to 0.015 THz.

Imaging Experimental Setup:
Experimental verification of the produced THz lens was performed using an in-house THz continuous-wave imaging setup. As a source of linearly polarised THz radiation, we used a BWO (GIP RAS) operating at a frequency of 327 GHz with a beam spot size as shown in Figure 1c. The detector (Golay cell) was mounted on motorised linear translation stages, which enabled a 3D pixel-by-pixel scan of the THz field intensity[53]. For THz imaging experiments, a solid immersion lens was integrated into the system. In a THz imaging experiment, a solid immersion lens was integrated into the system[14, 54]. The device showed an exponential change in transmission that stabilised and came to a plateau within several minutes. It is important to note that after several minutes of waiting, the cell was run for several hours until the x-y and x-z scans were completed. The reproducibility test states that the intensity values are the same for complete x-y and x-z scans taken at the same voltage during 2^{nd} and subsequent cycles.

THz propagation simulation: For numerical simulation of the Field interaction with the FZP, COMSOL Multiphysics Software was applied. The quasi-3D finite-element frequency-domain (FEFD) method was used for modelling the optical element with rotational symmetry with respect to the optical axis. The simulation volume was restricted using perfectly matched layers as absorbing boundaries. In the simulation, we implemented an infinitely thin 2D object with varying surface conductivity as a zone-plate material.

Acknowledgements
The authors would like to acknowledge the Clover Initiative. AVR, MGB, and AVA would like to acknowledge the Ministry of Science and Higher Education (FSMG-2025-0005, Imaging Experiments). AVR, MIP, and MGB acknowledge the Russian Science Foundation grant (Project No. 24-79-00143; Spectroscopy Measurements). GMK acknowledges a Russian Science Foundation grant (project No 25–79–10280; THz waveguiding delivery experiment). NIR, AAM, YGG, and AGN acknowledge the Russian Science Foundation grant (project No. 22-13-00436; Synthesis of SWCNTs).

Data availability
The data that support the plots in this study and other findings of this study are available from the corresponding author upon reasonable request.

Contributions

Accepted Manuscript

ACCEPTED ARTICLE PREVIEW

Arina V. Radivon: Writing - review & editing, Writing - original draft, Investigation, Formal analysis, Data curation. **Gleb M. Katyba**: Writing - review & editing, Writing - original draft, Investigation, Formal analysis, Data curation, Supervision. **Nikita I. Raginov**: Writing - original draft, Investigation, Resources. **Aram A. Mkrtchyan**: Writing - original draft,Writing - review & editing, Investigation, Resources. **Aleksey V. Chernykh**: Writing - original draft,Writing - review & editing, Investigation, Resources. **Ignat I. Rakov**: Writing - original draft,Writing - review & editing, Investigation, Resources. **Maksim I. Paukov**: Writing - original draft,Writing - review & editing, Investigation, Resources. **Mikhail S. Mironov**: Writing - original draft,Writing - review & editing, Investigation, Resources. **Mikhail V. Shashkov**: Writing - original draft,Writing - review & editing, Investigation, Resources. **Andrey A. Vyshnevyy**: Writing - original draft,Writing - review & editing, Investigation. **Demyan D. Rybnikov**: Writing - review & editing, Investigation. **Darya R. Ilyenkova**:Writing - review & editing, Investigation. **Gennadiy A. Komandin**: Writing - review & editing, Writing - original draft, Investigation, Formal analysis, Data curation, Supervision. **Kirill I. Zaytsev**: Writing - review & editing, Writing - original draft, Supervision, Project administration. **Yuriy G. Gladush**: Writing - review & editing, Writing - original draft, Supervision, Project administration. **Nikolay V. Petrov**: Writing - review & editing, Writing - original draft, Supervision, Project administration. **Albert G. Nasibulin**: Writing - review & editing, Writing - original draft, Supervision, Project administration. **Aleksey V. Arsenin**: Writing - review & editing, Writing - original draft, Supervision, Project administration. **Valentyn Volkov**: Writing - review & editing, Writing - original draft, Supervision, Project administration. **Dmitry V. Krasnikov**: Resources, Writing - review & editing, Writing - original draft, Supervision, Project administration. **Maria G. Burdanova**: Resources, Writing - review & editing, Writing - original draft, Formal analysis, Data curation, Supervision, Project administration. All authors commented on the manuscript.

Conflict of interests The authors declare no conflict of interest.

Corresponding author Correspondence to M.G. Burdanova.

Accepted Manuscript

References

[1] Beard, M. C., Turner, G. M. & Schmuttenmaer, C. A. Terahertz Spectroscopy. *The Journal of Physical Chemistry B* **106**, 7146–7159 (2002).

[2] Jepsen, P. U., Cooke, D. G. & Koch, M. Terahertz spectroscopy and imaging – Modern techniques and applications. *Laser & Photonics Reviews* **5**, 124–166 (2011).

[3] Novikova, T. I. et al. Statistical features of the response of a superconducting hot-electron bolometer to extremely weak terahertz pulses of picosecond and nanosecond duration. *Applied Physics Letters* **125**, 124004 (2024).

[4] Kovalev, S. et al. Terahertz signatures of ultrafast Dirac fermion relaxation at the surface of topological insulators. *npj Quantum Materials* **6**, 84 (2021).

[5] Paukov, M. I. et al. Ultrafast dynamics of excitons and charge carriers in Van der Waals WS2 nanotubes. *Materials Today Chemistry* **36**, 101886 (2024).

[6] Amenabar, I., Lopez, F. & Mendikute, A. In Introductory Review to THz Non-Destructive Testing of Composite Mater. *Journal of Infrared, Millimeter, and Terahertz Waves* **34**, 152–169 (2013).

[7] Kemp, M. C. et al. Security applications of terahertz technology. Proceedings of the Terahertz for Military and Security Applications. Orlando, FL, USA: SPIE, 2003, 44–52.

[8] Kolinko, V. G. et al. A passive millimeter-wave imaging system for concealed weapons and explosives detection (Invited Paper). Proceedings of the Optics and Photonics in Global Homeland Security. Orlando, FL, USA: SPIE, 2005, 85–92.

ACCEPTED ARTICLE PREVIEW

[9] Yang, X. et al. Biomedical Applications of Terahertz Spectroscopy and Imaging. *Trends in Biotechnology* **34**, 810–824 (2016).

[10] Janssens, K. et al. Photon-Based Techniques for Nondestructive Subsurface Analysis of Painted Cultural Heritage Artifacts. *Accounts of Chemical Research* **43**, 814–825 (2010).

[11] Laikin, M. Lens Design. 4th edn. (Boca Raton, FL: CRC Press, 2007).

[12] Chernomyrdin, N. V. et al. Wide-aperture aspherical lens for high-resolution terahertz imaging. *Review of Scientific Instruments* **88**, 014703 (2017).

[13] Lo, Y. H. & Leonhardt, R. Aspheric lenses for terahertz imaging. *Optics Express* **16**, 15991–15998 (2008).

[14] Zhelnov, V. A. et al. Hemispherical rutile solid immersion lens for terahertz microscopy with superior 0.06–0.11λ resolution. *Advanced Optical Materials* **12**, 2300927 (2024).

[15] Yu, Q. et al. Terahertz bistatic three-dimensional computational imaging of hidden objects through random media. *Scientific Reports* **14**, 6147 (2024).

[16] Daniel, L. et al. Low-THz radar, lidar and optical imaging through artificially generated fog. Proceedings of the International Conference on Radar Systems (Radar 2017). Belfast: IEEE, 2017, 1–4.

[17] Wu, Y. et al. Graphene terahertz modulators by ionic liquid gating. *Advanced Materials* **27**, 1874–1879 (2015).

[18] Sarfraz, S. M. A. et al. Electrolyte gated graphene terahertz amplitude modulators. *Applied Physics Letters* **124**, 071114 (2024).

[19] Kopylova, D. S. et al. Electrochemical enhancement of optoelectronic performance of transparent and conducting single-walled carbon nanotube films. *Carbon* **167**, 244–248 (2020).

[20] Burdanova, M. G. et al. A review of the terahertz conductivity and photoconductivity of carbon nanotubes and heteronanotubes. *Advanced Optical Materials* **9**, 2101042 (2021).

[21] Khabushev, E. M. et al. Machine learning for tailoring optoelectronic properties of single-walled carbon nanotube films. *The Journal of Physical Chemistry Letters* **10**, 6962–6966 (2019).

[22] Katyba, G. M. et al. Tunable THz flat zone plate based on stretchable single-walled carbon nanotube thin film. *Optica* **10**, 53–61 (2023).

[23] Radivon, A. V. et al. Expanding THz vortex generation functionality with advanced spiral zone plates based on single-walled carbon nanotube films. *Advanced Optical Materials* **12**, 2303282 (2024).

[24] Kaskela, A. et al. Aerosol-synthesized SWCNT networks with tunable conductivity and transparency by a dry transfer technique. *Nano Letters* **10**, 4349–4355 (2010).

[25] Hecht, E. Optics. 5th edn. (Upper Saddle River, NJ: Pearson, 2015).

[26] Saito, R. et al. Gate modulated Raman spectroscopy of graphene and carbon nanotubes. *Solid State Communications* **175–176**, 18–34 (2013).

[27] Kang, D. H. et al. Oxygen-induced p-type doping of a long individual single-walled carbon nanotube. *Nanotechnology* **16**, 1048–1052 (2005).

[28] Macutkevic, J. et al. Multi-walled carbon nanotubes/PMMA composites for THz applications. *Diamond and Related Materials* **25**, 13–18 (2012).

[29] Macutkevic, J. et al. Terahertz probing of onion-like carbon-PMMA composite films. *Diamond and Related Materials* **17**, 1608–1612 (2008).

Accepted Manuscript

ACCEPTED ARTICLE PREVIEW

[30] Nemat-Nasser, S. C. et al. Terahertz plasmonic composites. *Physical Review E* **75**, 036614 (2007).

[31] Novikov, I. V. et al. Multifunctional elastic nanocomposites with extremely low concentrations of single-walled carbon nanotubes. *ACS Applied Materials & Interfaces* **14**, 18866–18876 (2022).

[32] Zou, Q. et al. MXene-based ultra-thin film for terahertz radiation shielding. *Nanotechnology* **31**, 505710 (2020).

[33] Huang, Z. Y. et al. Graphene-based composites combining both excellent terahertz shielding and stealth performance. *Advanced Optical Materials* **6**, 1801165 (2018).

[34] Lin, Z. H. et al. Highly stable 3D $Ti_3C_2T_x$ MXene-based foam architectures toward high-performance terahertz radiation shielding. *ACS Nano* **14**, 2109–2117 (2020).

[35] Pavlou, C. et al. Effective EMI shielding behaviour of thin graphene/PMMA nanolaminates in the THz range. *Nature Communications* **12**, 4655 (2021).

[36] Rogozhkin, G. V. et al. Mechanically neutral and facile monitoring of thermoset matrices with ultrathin and highly porous carbon nanotube films. *Carbon* **230**, 119603 (2024).

[37] Georgieva, A., Belashov, A. V. & Petrov, N. V. Optimization of DMD-based independent amplitude and phase modulation by analysis of target complex wavefront. *Scientific Reports* **12**, 7754 (2022).

[38] Brossard, M. et al. Terahertz adaptive optics with a deformable mirror. *Optics Letters* **43**, 1594–1597 (2018).

[39] Vallés, A. et al. Broadband high-resolution terahertz single-pixel imaging. *Optics Express* **28**, 28868–28881 (2020).

[40] Leibov, L. et al. Speckle patterns formed by broadband terahertz radiation and their applications for ghost imaging. *Scientific Reports* **11**, 20071 (2021).

[41] Malevich, Y. et al. Very-large-scale reconfigurable intelligent surfaces for dynamic control of terahertz and millimeter waves. *Nature Communications* **16**, 2907 (2025).

[42] Wang, G. C. et al. Pump-wavelength sensitive terahertz spatiotemporal metasurface. *Advanced Optical Materials* **12**, 2301994 (2024).

[43] Lowry, S. N. et al. Spatial polarization modulation for terahertz single-pixel imaging. *IEEE Transactions on Terahertz Science and Technology* **14**, 386–394 (2024).

[44] Zhang, P. J. et al. Dynamic large-array terahertz imaging display based on high-performance 1D/2D tellurium homojunction modulators. *APL Photonics* **9**, 031301 (2024).

[45] Zhang, X. et al. Lensless imaging with a programmable Fresnel zone aperture. *Science Advances* **11**, eadt3909 (2025).

[46] Cherkasova, O. P. et al. Cellular effects of terahertz waves. *Journal of Biomedical Optics* **26**, 090902 (2021).

[47] Titova, L. V. et al. Intense THz pulses down-regulate genes associated with skin cancer and psoriasis: a new therapeutic avenue? *Scientific Reports* **3**, 2363 (2013).

[48] Katyba, G. M. et al. Sapphire photonic crystal waveguides for terahertz sensing in aggressive environments. *Advanced Optical Materials* **6**, 1800573 (2018).

[49] Rakić, A. D. et al. Sensing and imaging using laser feedback interferometry with quantum cascade lasers. *Applied Physics Reviews* **6**, 021320 (2019).

Accepted Manuscript

ACCEPTED ARTICLE PREVIEW

[50] Vorotyntsev, M. A. et al. Electrochemical and spectral properties of ferrocene (Fc) in ionic liquid: 1-butyl-3-methylimidazolium triflimide, [BMIM][NTf2]. concentration effects. *The Journal of Physical Chemistry B* **113**, 1085–1099 (2009).

[51] Tiago, G. A. O. et al. Application of Ionic Liquids in Electrochemistry—Recent Advances. *Molecules* **25**, 5812 (2020).

[52] Chen, C. C. & Huang, Y. S. Influence of crucible material on the thermal stability analysis of ionic liquid 1-butyl-3-methylimidazolium bis(trifluoromethylsulfonyl)imide. *Journal of Thermal Analysis and Calorimetry* **148**, 6731–6745 (2023).

[53] Ulitko, V. E. et al. Opal-based terahertz optical elements fabricated by self-assembly of porous SiO2 nanoparticles. *Optics Express* **29**, 13764–13777 (2021).

[54] Chernomyrdin, N. V. et al. Terahertz solid immersion microscopy: Recent achievements and challenges. *Applied Physics Letters* **120**, 110501 (2022).

Accepted Manuscript

ACCEPTED ARTICLE PREVIEW

Table of Contents/Graphical Abstract:

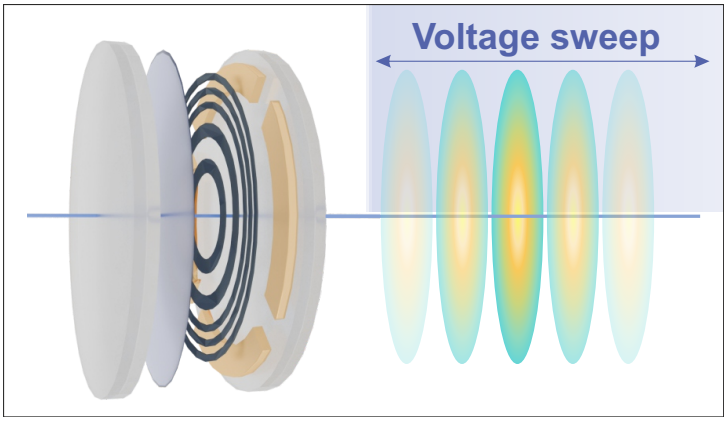

Accepted Manuscript

ACCEPTED ARTICLE PREVIEW

Supplementary information for: Gate-tunable FZP based on single-walled carbon nanotubes for terahertz applications

Arina V. Radivon Nikita I. Raginov Elizaveta G. Tsiplakova Aram A. Mkrtchyan Gleb M. Katyba Aleksey V. Chernykh Ignat I. Rakov Maksim I. Paukov Mikhail S. Mironov Mikhail V. Shashkov Andrey A. Vyshnevyy Demyan D. Rybnikov Darya R. Ilyenkova Gennadiy A. Komandin Kirill I. Zaytsev Yuriy G. Gladush Nikolay V. Petrov Albert G. Nasibulin Aleksey V. Arsenin Valentyn Volkov Dmitry V. Krasnikov Maria G. Burdanova

Accepted Manuscript

ACCEPTED ARTICLE PREVIEW

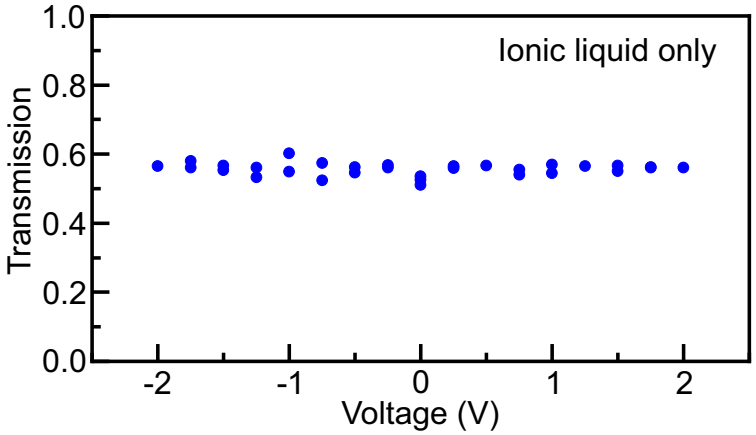

Figure S1: The transmission at 320 GHz as a function of voltage for ionic liquid squeezed between two quartz substrates.

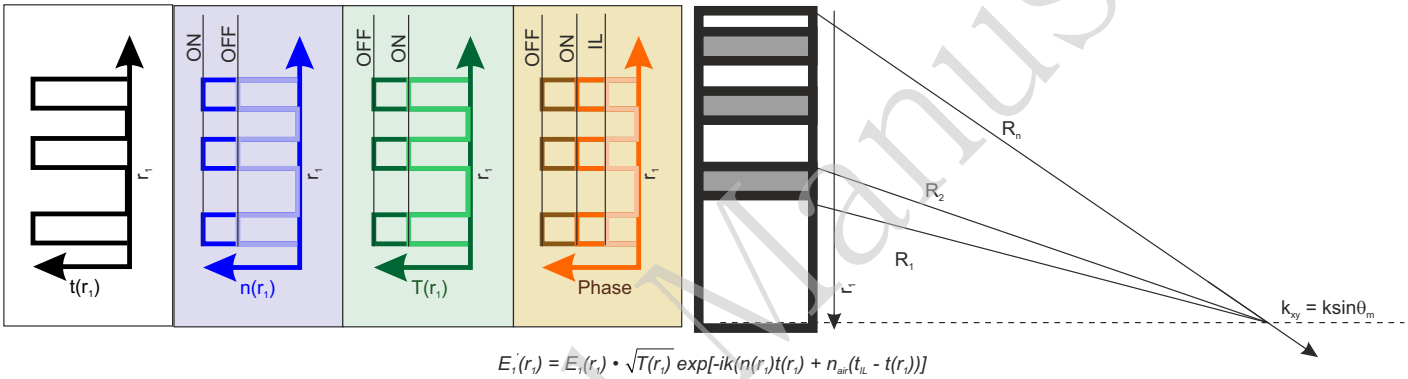

Figure S2: The general explanation of the change of the intensity using analytical Rayleigh–Sommerfeld diffraction theory. From the left to right: thickness, refractive index, transmission and phase profiles along with radial direction.

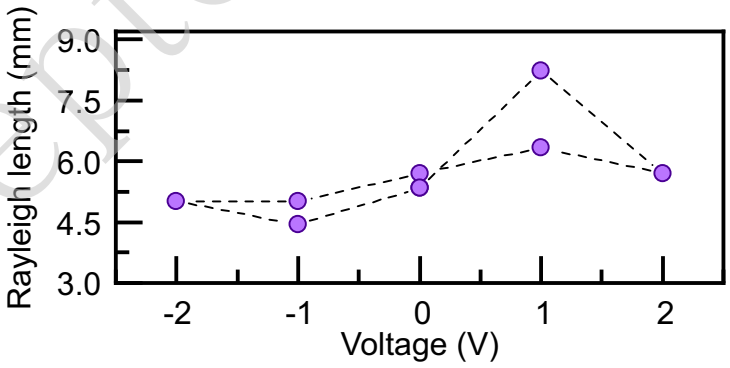

Figure S3: Rayleigh length parameter as a function of voltage.

Accepted Manuscript

ACCEPTED ARTICLE PREVIEW

1. Shadow mask for gold contact deposition

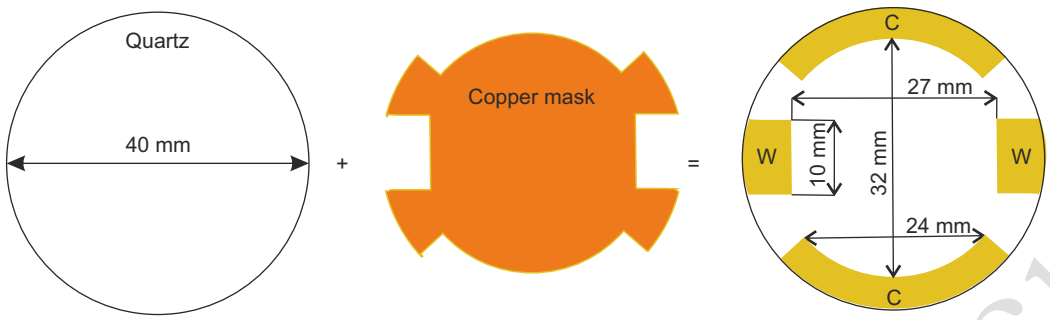

2. CNT pattern following the diameters in table

n	d_n(mm)
1	8.609242
2	12.24403
3	15.07951
4	17.50842
5	19.68188
6	21.67685
7	23.53877
8	25.29703
9	26.9719
10	28.57806

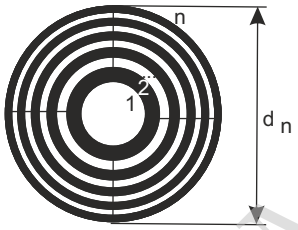

3. Dry-transfer CNT on Quartz with gold contacts

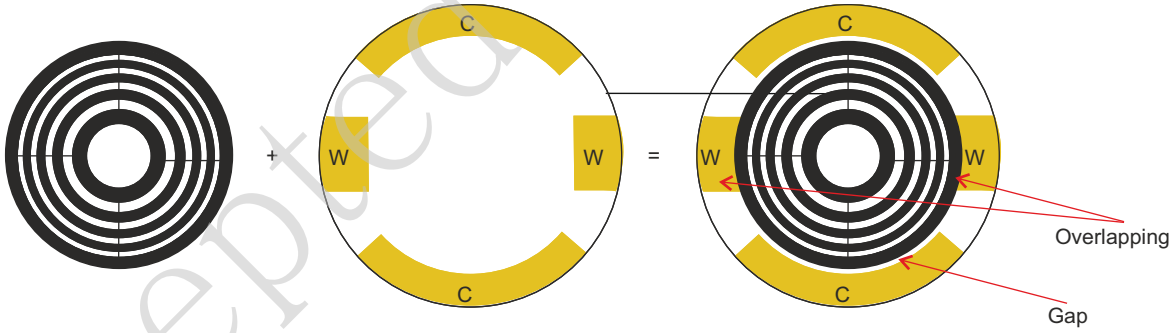

4. Coverage with ionic liquid and encapsulation

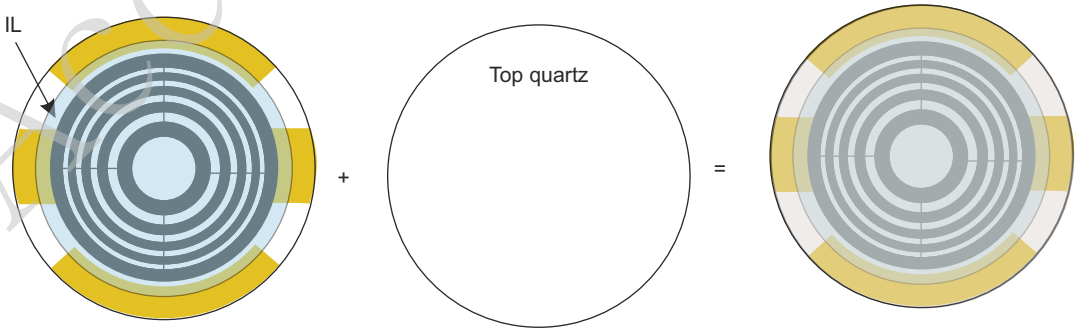

Figure S4: The main fabrication steps of electrochemically gated FZP. "C" denotes the counter electrode, while "W" denotes the working electrode.

Accepted Manuscript

ACCEPTED ARTICLE PREVIEW

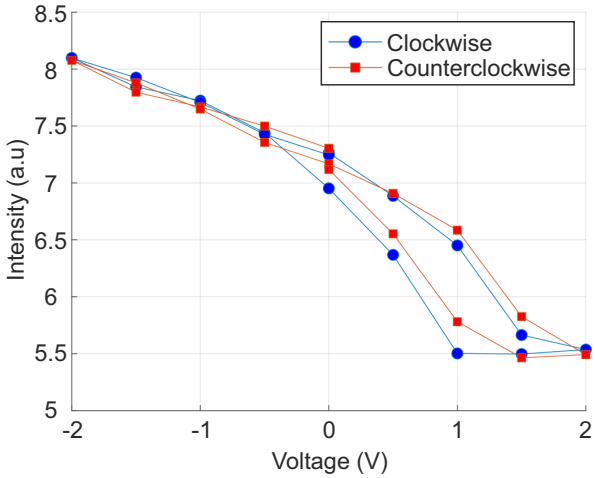

Figure S5: Change in the focal spot intensity of the lens for the voltage bias in the range of -2 to 2 V with the step of 0.5 V for voltage applied clockwise and counterclockwise.

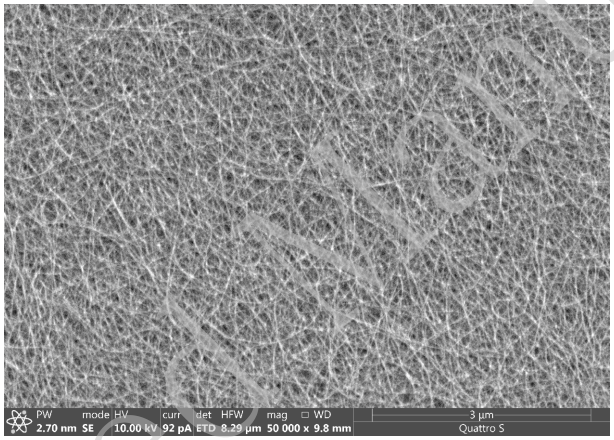

Figure S6: The SEM image of a pristine SWCNT film shows the morphology of randomly oriented SWCNTs composed of FZP.

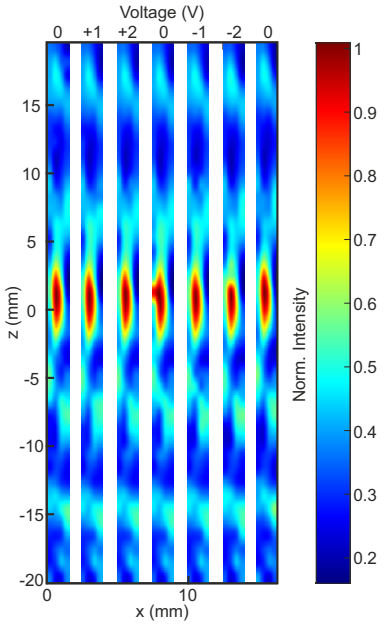

Figure S7: The intensity images along beam propagation direction.

Accepted Manuscript

ACCEPTED ARTICLE PREVIEW

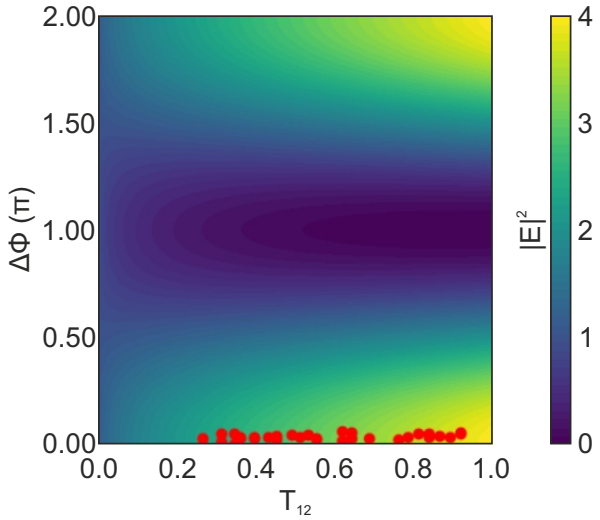

Figure S8: The interference of two coherent beams as a function of the phase change ($\Delta\phi_{12} = \phi_1 - \phi_2$)and the squared amplitude ratio $T_{12} = |A_1 A_2^{-1}|$. The points correspond to the values obtained in the experiments, illustrating the relationship between phase variations and amplitude effects on the resulting interference pattern.

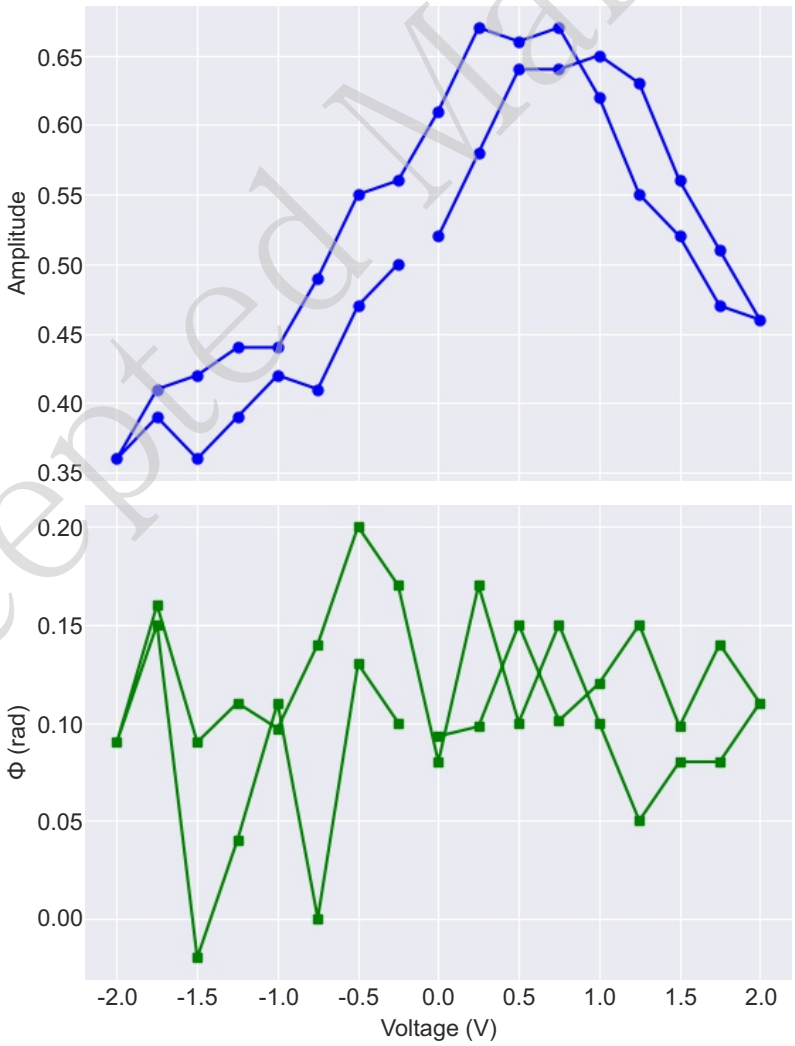

Figure S9: Amplitude and phase of transmission function modulated by the applied voltage.

Accepted Manuscript